Nearfield Anisotropic Mesh Adaptation for the Third AIAA Sonic Boom Workshop

Julien Vanharen,* Adrien Loseille,† and Frédéric Alauzet‡
INRIA Paris-Saclay, 91120 Palaiseau, France

Michael A. Park§
NASA Langley Research Center, Hampton, VA 23681, USA

Sonic boom prediction is critical for the development of low-boom supersonic aircraft and encouraging a replacement of the overland commercial supersonic ban with a certification standard. The Third AIAA Sonic Boom Workshop nearfield test cases provide a unique opportunity to review anisotropic adaptive-mesh strategies for complex geometries with important propulsion interaction effects. Anisotropic metrics formulated to control estimated Mach interpolation and integrated nearfield pressure signature (goal-oriented) errors are compared with the results obtained on workshop-provided meshes. Detailed flow solutions and mesh renderings are combined with computational schlieren images to reveal the complex interactions present in a shock-plume interaction wind tunnel model and a prototype of the Low-Boom Flight Demonstrator. A favorable comparison of independent implementations of the entire simulation process provides evidence that each process is implemented correctly and sets a solid foundation for confidence in the nearfield prediction of each method.

Nomenclature

α	=	angle of attack
Π_h	=	piecewise linear representation
φ	=	offtrack angle
Ψ and Ψ_h	=	continuous and discrete residual operators
Ω	=	domain or volume
$\#DOF$	=	number of control volumes (degrees of freedom)
$\mathcal{C}(\mathcal{M})$	=	complexity of the metric
d	=	number of domain dimensions
$\mathcal{E}$	=	error model
$\mathcal{F}^E$ and $\mathcal{F}^V$	=	inviscid and viscous fluxes
H	=	altitude
$\mathcal{H}_{Opt}$	=	optimal mesh
$\mathcal{H}$	=	Hessian
J	=	scalar function
L	=	reference body length
L^p	=	p-norm
M	=	freestream Mach number
$\mathcal{M}$	=	anisotropic metric field
$\mathcal{N}$	=	complexity constraint
p and p_∞	=	local and freestream pressure
$\mathcal{P}$	=	mean of the L^2-norm of normalized pressure ratio
Re	=	Reynolds number
T	=	temperature

*INRIA Postdoctoral Fellow, GAMMA Team
†Research Scientist, GAMMA Team, Member AIAA
‡Research Scientist, GAMMA Team, Member AIAA
§Research Scientist, Computational AeroSciences Branch, AIAA Associate Fellow

u	=	sensor field for interpolation-error control
W	=	solution
W^*	=	adjoint state

I. Introduction

The quantification and control of discretization error for the Reynolds-averaged Navier–Stokes (RANS) equations is critical to obtaining reliable simulation results. Recent progress has matured anisotropic mesh adaptation processes to provide automatic control of estimated errors, which have been verified by code-to-code comparison [1–4]. Alauzet and Loseille [5] documented the dramatic progress made in the last decade for anisotropic solution-adaptive methods to resolve simulations with shocks and boundary layers.

Complex low-boom configurations are particularly challenging due to interaction of weak shocks and expansions with boundary layer and propulsion effects that are difficult to predict numerically. Assessing the nearfield sonic boom signatures with both inviscid and viscous flows is still a challenge. The Third AIAA Sonic Boom Workshop (SBPW3) is a unique occasion to assess and compare the performance of different solvers, approaches, and meshing techniques to resolve these features. Anisotropic mesh adaptation is designed to automatically resolve the anisotropic features of the physical phenomena under study. In this respect, the computation of near field signatures of supersonic aircraft have been one of the primary field of applications (and successes) of anisotropic mesh adaptation [6, 7].

The adaptive computations use Hessian-based interpolation error control and goal-oriented approaches based on fully unstructured meshes. Both of them naturally yield an anisotropic prescription of optimal meshes that are independent of geometric complexity. We control the interpolation error of Mach number in the L^p norm or control estimated errors in a nearfield pressure functional. Controlling functional error is referred as the goal-oriented approach. For each case, sequences of meshes with an increasing complexity (control volumes) are generated. These mesh adaptation frameworks are composed of a flow solver, a metric-based error estimate, and a mesh adaptation algorithm. These frameworks are applied to the shock-plume and low-boom flight demonstrator configurations of SBPW3.

II. Flow solver

Two flow solvers are used for nearfield predictions. They share many high-level similarities, i.e., they combine finite-volume convection and finite-element diffusion terms. These solvers differ in the details of the convection terms and the solution update schemes. Both methods have extensive application to nearfield sonic boom modeling, including participation in previous sonic boom workshops.

A. Wolf

Wolf is a vertex-centered (flow variables are stored at vertices of the mesh) mixed finite-volume and finite-element RANS solver on unstructured meshes composed of triangles in 2D and tetrahedra in 3D. The convective terms are solved by the finite-volume method on the dual mesh composed of median cells. It uses a Harten, Lax, and van Leer Contact HLLC approximate Riemann solver [8] to compute the fluxes at the cell interfaces. Second-order space accuracy is achieved through a piecewise linear interpolation based on the Monotonic Upwind Scheme for Conservation Law (MUSCL) procedure, which uses a particular edge-based formulation with upwind elements [6]. A specific low dissipation scheme combines centered (edge) and upwind (element) gradients. A dedicated slope limiter is employed to damp or eliminate spurious oscillations that may occur in the vicinity of discontinuities. The viscous terms are solved by the P^1 Galerkin Finite Element Method (FEM), which provides second-order accuracy.

The implicit temporal discretization considers the backward Euler time-integration scheme. At each time step, the linear system of equations is approximately solved using a Symmetric Gauss-Seidel (SGS) implicit solver and local time stepping to accelerate the convergence to steady state. A Newton method based on the SGS relaxation is very attractive because it uses an edge-based data structure that can be efficiently parallelized. For the turbulence model, the Spalart-Allmaras (SA) model [9] is loosely-coupled to the mean-flow equations, where the mean-flow and turbulence model equations are relaxed in an alternating sequence. The flow solver, Wolf, is thoroughly detailed in [6, 10] with a complete bibliography.

The following *crucial* choices are made to solve the compressible Navier-Stokes equations. The SGS relaxation iterates until the residual of the linear system is reduced by one or two orders of magnitude. A Breadth First Search renumbering proves to be the more effective for the convergence of the implicit method and the overall efficiency. Fully

differentiating the HLLC approximate Riemann solver and the viscous terms increases the nonlinear convergence rate. To achieve convergence of the nonlinear system of algebraic equations to steady state with high efficiency, automation, and robustness, it is mandatory to have a clever strategy to specify the Courant Friedrichs Lewy (CFL) condition. The CFL evolution depends on the convergence of the linear system and on the evolution of the solution at each time step. A similar strategy is the Hierarchical Adaptive Nonlinear Iteration Method (HANIM) [11].

The adjoint state computation is needed for goal-oriented error estimates. The adjoint system is the transposed flow solver implicit matrix (without the mass matrix) and the exactly differentiated functional (i.e., drag, lift, nearfield signature integral). For viscous flows, viscosity and the stress tensor are exactly differentiated. For a consistent goal-oriented mesh adaptation, the adjoint linear system must be converged to machine zero. In our applications, we generally converge the linear system by eight to twelve orders of magnitude to obtain an accurate adjoint state for mesh adaptation. The adjoint linear system is significantly stiffer than the flow solver linear system, which includes a mass matrix. For inviscid flows, the adjoint linear system is routinely solved with a restarted Generalized Minimum Residual (GMRES) [12] preconditioned with LUSGS relaxation. The adjoint linear system is more difficult to converge for RANS, particularly for drag and high-lift prediction problems.

Increasing Krylov vectors to 1,000 was only able to reduce the adjoint residual three to five orders of magnitude in 10,000 iterations. Large numbers of Krylov space vectors have large memory requirements, which make them unusable in practice. A key improvement is the use of a stronger preconditioner to yield a restarted GMRES preconditioned with 10 passes of SGS (forward and backward sweeps). With the preconditioner, the adjoint linear system converges in less than 100 iterations with 100 Krylov vectors. For highly refined 3D cases, around 200 iterations may be required with a Krylov space of 250 vectors.

B. FUN3D-FV

Fully Unstructured Navier-Stokes Finite-Volume (FUN3D-FV) [13, 14] is a Navier-Stokes solver where the flow variables are stored at the vertices of the mesh. At interfaces between neighboring control volumes, the inviscid fluxes are computed using the Roe approximate Riemann solver [15] based on the values on either side of the interface. For second-order accuracy, interface values are extrapolated from the vertices with gradients computed at the mesh vertices. These gradients are reconstructed with an unweighted least-squares technique [13]. The interface values are limited with the method of van Leer [16].

The full viscous fluxes are discretized using a finite-volume formulation where the required velocity gradients on the dual faces are computed using the Green-Gauss theorem. On tetrahedral meshes, this is equivalent to a Galerkin type approximation. The solution at each time step is updated with a backward Euler time-integration scheme. At each time step, the linear system of equations is approximately solved with a multicolor point-implicit procedure [17]. Local time-step scaling is employed to accelerate convergence to steady state. The SA turbulence model is loosely-coupled to the meanflow equations, where the meanflow and turbulence model equations are relaxed in an alternating sequence.

The SA turbulence model requires the distance from every node to the nearest noslip boundary. The standard wall distance calculation in FUN3D-FV finds the nearest surface node and then searches adjacent triangles to see if they are closer than the closest surface node. The standard wall distance method is inaccurate if the closest triangle is not adjacent to the closest surface node. To provide an accurate wall distance, which is critical to the SA model, an alternative method is used on adapted meshes. The alternative method encloses each surface triangle in a bounding box. These bounding boxes are stored in an Alternating Digital Tree (ADT) [18] for fast searches. The alternative wall distance method finds the closest surface triangle for adapted unstructured meshes.

III. Metric-Based Error Estimates

In the mesh adaptation process, the metric field $(\mathcal{M}(\mathbf{x}))_{\mathbf{x}\in\Omega}$ used to prescribe the new adapted mesh $\mathcal{H}$. An $\mathcal{M}$ is automatically deduced from the actual solution (and adjoint state) for different error estimates [5]. The goal is to find the optimal mesh $\mathcal{H}_{Opt}$ that minimizes the given error model E for a fixed number of elements $C(\mathcal{H}_{Opt}) = N$:

$$\mathcal{H}_{Opt} = \underset{C(\mathcal{H})=N}{\operatorname{argmin}} E(\mathcal{H}).$$

This problem can be analytically solved by recasting it in the continuous mesh theoretical framework [19, 20]. The goal is to find the optimal continuous mesh $\mathcal{M}_{Opt}$ that minimizes the given continuous error model $\mathcal{E}$ for a fixed continuous mesh complexity $C(\mathcal{M}) = \mathcal{N}$:

$$\mathcal{M}_{Opt} = \underset{C(\mathcal{M})=\mathcal{N}}{\operatorname{argmin}} \mathcal{E}(\mathcal{M}).$$

The continuous mesh complexity is the continuous counterpart of the discrete mesh size (number of points or elements) and is used to prescribed the mesh size during the adaptation process. The complexity is computed in [5, 21] by:

$$C(\mathcal{M}) = \int_\Omega \sqrt{\det \mathcal{M}}\, \mathrm{d}\Omega\,.$$

In this work, we consider interpolation-based error estimates based on a control of the interpolation error in L^p-norm and goal-oriented error estimate based on the a priori analysis of Refs. [22, 23].

A. Interpolation-Based Error Estimate

The most natural and straight forward approach is to control the interpolation error of a sensor field $u = f(W)$ [21, 24, 25], which is defined from solution W. Given a continuous sensor u, it is represented by its discrete nodal values on the mesh $u_i = u(x_i)$ and its piecewise linear representation $\Pi_h u$ on mesh $\mathcal{H}$. The L^p-norm of the interpolation error of the sensor field u is stated as

$$E(\mathcal{H}) = \left(\int_\Omega |u - \Pi_h u|^p \, \mathrm{d}\Omega \right)^{1/p}.$$

Interpolation-based mesh adaptation enables control of the global interpolation error of the given sensor field. Under certain assumptions, we can prove that this approach also controls the approximation error [7]. The analytical expression of the optimal continuous mesh $\mathcal{M}_{Opt}$ in L^p-norm is given by Ref. [6]:

$$\mathcal{M}_{L^p}(\mathbf{x}) = \mathcal{N}^{\frac{2}{d}} \left(\int_\Omega \det(|H_u|)^{\frac{p}{2p+d}} \, \mathrm{d}\Omega \right)^{-\frac{2}{d}} \det(|H_u(\mathbf{x})|)^{-\frac{1}{2p+d}} \, |H_u(\mathbf{x})|\,, \tag{1}$$

where $\mathcal{N}$ is the complexity, d is the space dimension and H_u is the Hessian of the sensor u computed using a double L^2-projection method [6, 26]. A recursive application of gradient reconstruction is used to form the second-derivative Hessian terms. The gradient is computed in each element and a volume-weighted average is collected at each vertex. The second-derivative Hessian terms are formed by computing the reconstructed gradients of the gradients formed in the first pass. The mixed derivative terms of the Hessian are averaged. A special boundary treatment is employed, where the reconstructed Hessian on the boundary is replaced with an extrapolation from neighboring interior vertices, which have a well-formed stencil. The Hessian is decomposed into eigenvalues and eigenvectors. The metric is formed by recombining the absolute value of the eigenvalues with the eigenvectors to ensure the metric is symmetric positive definite [27]. In this paper, we consider the L^2- and the L^4-norm of the interpolation error of the Mach sensor field. Controlling the interpolation error of the Mach sensor field implicitly controls the interpolation error of all primal variables.

B. Goal-Oriented Error Estimate

Interpolation-based adaptation is efficient to control the interpolation error of a sensor field but it ignores the nonlinear dependency of the solution W to the mesh and the considered system of equations. Interpolation error control improves the overall solution but ignores the ultimate goal of the simulation: accurate engineering outputs. Accurate simulation results can be achieved by considering goal-oriented error estimates where the nonlinear dependency is taken into account by using the adjoint state W^*.

The objective is to minimize the approximation error in the computation of a given scalar functional $J(W)$:

$$E^{go}(\mathcal{H}) = |J(W) - J(W_h)| = |\delta J|.$$

A specific goal-oriented error analysis analytically derives an optimal metric field from the adjoint and primal fields. This analysis has been performed for inviscid flows and has shown excellent results [22]. The same analysis was recently performed for laminar viscous flows and showed very good results [23]. The main advantage of these estimates, in comparison to other goal-oriented error estimates, is that the anisotropy of the mesh appears naturally within the continuous mesh framework [19, 20] and they provide a direct analytical expression for the optimal mesh. In this error estimation problem, the approximation error on the functional can be decomposed into an implicit error term and an interpolation error term:

$$|\delta J| = |J(W) - J(W_h)| = |(g, W - W_h)| \leq |(g, W - \Pi_h W)| + |(g, \Pi_h W - W_h)|\,. \tag{2}$$

The interpolation error term is easily estimated using Eq. (1). For the implicit term, we demonstrate [22, 23] that:

$$|(g, W_h - \Pi_h W)| \approx (\Psi(W) - \Psi_h(\Pi_h W),\, \Pi_h W^*)\,, \tag{3}$$

where Ψ and Ψ_h are the continuous and discrete operators of the considered problem. We use a finite-element framework to accurately analyze the implicit error term involved in the Navier-Stokes equations. We denote the inviscid fluxes $\mathcal{F}^E(W)$ and the viscous fluxes $\mathcal{F}^V(W)$. Starting from Eq. (3), both inviscid and viscous fluxes are linearized with respect to the solution W and its gradients ∇W. By integrating by parts (and omitting the boundary terms), this expression is obtained [23, 28]:

$$\begin{aligned}
|(g, W_h - \Pi_h W)| &\approx \int_\Omega \left|W^*\right| \left|\nabla \cdot (\mathcal{F}^E(W) - \mathcal{F}^E(\Pi_h W)) - \nabla \cdot (\mathcal{F}^V(W) - \mathcal{F}^V(\Pi_h W))\right| \mathrm{d}\Omega \\
&\leq \left| \int_\Omega \sum_i \nabla_{x_i} \left[\frac{\partial \mathcal{F}_i^E}{\partial W} (W - \Pi_h W) \right] W^* + \sum_{i,j} \nabla_{x_i} \left[\frac{\partial \mathcal{F}_i^V}{\partial \nabla_{x_j} W} \nabla_{x_j} (W - \Pi_h W) \right] W^* \,\mathrm{d}\Omega \right| \\
&\leq \int_\Omega \left| \sum_i \frac{\partial \mathcal{F}_i^E}{\partial W} \nabla_{x_i} W^* + \sum_{i,j} \frac{\partial \mathcal{F}_i^V}{\partial \nabla_{x_j} W} \nabla_{x_i, x_j} W^* \right| \left| W - \Pi_h W \right| \mathrm{d}\Omega\,.
\end{aligned} \tag{4}$$

This implicit error estimate is a weighted sum of interpolation errors in the L^1-norm on the conservative variables where the weights depend on the gradient and the Hessian of the adjoint state and on the convective and viscous fluxes. From Eq. (2), the interpolation error term is added to have the approximate error estimate:

$$|J(W) - J(W_h)| \leq \int_\Omega \left| \frac{\partial j}{\partial W} + \sum_i \frac{\partial \mathcal{F}_i^E}{\partial W} \nabla_{x_i} W^* + \sum_{i,j} \frac{\partial \mathcal{F}_i^V}{\partial \nabla_{x_j} W} \nabla_{x_i, x_j} W^* \right| \left| W - \Pi_h W \right| \mathrm{d}\Omega\,.$$

The analytical expression of the optimal goal-oriented continuous mesh, Eq. (1), is available via this summation.

IV. Mesh Adaptation Algorithms

Two adaptive remeshers are used to realize the adapted mesh from the interpolation-based or goal-based metrics. They both use local mesh operations to guarantee a valid mesh is available to continue the solution adaptive process.

A. `Feflo.a` Adaptive Remesher

The `Feflo.a` adaptive remesher is based on a generalization of classic local operators (e.g., insertion, collapse, swap, vertex movement). The generalized operator recasts classic operators in a cavity framework [29–31]. This cavity operator allows mesh modifications that are not possible with a sequential application of the classic operators. The metric conformity of the mesh is enhanced by the cavity operator because it automatically combines multiple classic operations in a single operation to escape local minima that trap classic operators. In addition, the execution time of the cavity operator is reduced over classic operators and becomes independent of the mesh modification. The unit speed is approximately 20, 000 operations per second on Intel i7 architecture at 2.7 GHz. For robustness purpose, both the surface and the volume mesh are adapted simultaneously, and each local modification is checked to verify that a valid mesh is obtained. For the volume, the validity consists in checking that each newly created element has a strictly positive volume. For the surface, the validity is checked by ensuring that the deviation of the geometric approximation with respect to a reference surface mesh remains within a given tolerance [32].

B. `refine` Adaptive Remesher

The `refine` mesh adaptation package is designed to output a unit mesh [19] in a provided metric field from an initial mesh that conforms to the geometry. Geometry is accessed by `refine` through the EGADS [33] application programming interface.* A set of geometry metric constraints are inferred from the geometry model [3]. These constraints are satisfied on the initial mesh and remain active during all subsequent adapted meshes.

`refine` uses the combination of classic split, collapse, and element swap operations in a distributed-memory parallel environment [35]. Some of these classic operators are undergoing replacement with cavity operators [29] to allow more

*Or the EGADSlite [34] version of EGADS, which is a lightweight ANSI-C version of the EGADS functions required by the initial and adaptive mesh process, where the target is any high-performance computing equipment currently in use, including graphic processing units (GPUs).

complex element connectivity changes that escape the element validity constraints of sequential application of classic operators. Nonsmooth optimization based on Freitag and Ollivier-Gooch [36] relocates vertices for poorly shaped elements. Vertex relocation is performed to improve adjacent element shape with a convex combination of ideal vertex locations [37] for elements with medium shape measures. As elements approach an ideal shape in the metric, pliant smoothing of Bossen and Heckbert [38] is used to drive edge length distributions toward unity.

V. Numerical Results

Two nearfield test cases are provided by SBPW3. The first case deals with the simulation of a wind tunnel test for assessment of the capability to simulate shock-plume interaction in the NASA Ames 9×7 wind tunnel [39, 40]. Multiple configurations were tested in the wind tunnel campaign, and the biconvex shock generator was selected for SBPW3. The computations use interpolation-based (L^2- and L^4-norms) and goal-oriented error estimates. The second case deals with the computation of the C608 Low-Boom Flight Demonstrator using the interpolation-based (L^2-norm) error estimates. The C608 is a modified preliminary design of the evolving Lockheed Martin X-59 QueSST for NASA's Low-Boom Flight Demonstrator program.

A. Biconvex 9×7 Shock-Plume Experiment

Figure 1 shows the geometry of the wind tunnel model and support hardware. All the computations are carried out with the physical parameters listed in Table 1. The engine plenum total pressure ratio to freestream static pressure is equal to 8.0 and the engine plenum total temperature ratio to freestream static temperature is equal to 1.768.



Fig. 1 Biconvex 9×7 geometry.

Table 1 Flow characteristics for the biconvex 9×7 test case.

Characteristic	Symbol	Value	Units
Mach	M	1.3	$[-]$
Angle of attack	α	0.0	$[-]$
Temperature	T	374	$[R]$
Reynolds number per inch	Re	376850	$[-]$

Mach number interpolation error is controlled in the L^2- or L^4-norm in a sequence of 35 meshes. The goal-oriented approach uses a sequence of 30 meshes with the pressure integral on a cylinder of a radius $R = 15$ $[in]$ along the x-axis between an angle from 0° to 30° as the function of interest. Five meshes at a fixed complexity were generated and then the prescribed complexity is doubled for the next five meshes. The prescribed complexities are [0.2M, 0.4M, 0.8M, 1.6M, 3.2M, 6.4M, 12.8M]. The final meshes, respectively, for the L^2, L^4 and goal-oriented approaches are composed, respectively, of 26.9M, 26.3M and 13.0M vertices (160M, 156M and 77M tetrahedra). To illustrate the ability of anisotropic unstructured mesh adaptation to resolve the key features of the solution regardless of scale, the final mesh for the L^4-norm Mach interpolation-error control is shown in Fig. 2. The pressure ratio $\Delta p/p_\infty$ and mesh are shown on the symmetry plane, geometry, and a cut throughout the volume at an x-constant plane. The range of the colormap for the pressure ratio is uniform from $\Delta p/p_\infty = -0.4$ $[-]$ (blue) to $\Delta p/p_\infty = +0.4$ $[-]$ (red). The gray color represents a zero pressure ratio. The support sting creates an oblique shock. The boundary layer, shear layer surrounding the plume, biconvex shock generator wake, and biconvex shock generator tip vortex are all tracked by

the anisotropic adapted mesh. The tetrahedral sting wake refinement is seen adjacent to the symmetry plane on the x-constant intersection plane. The shocks from biconvex shock generator are weaker sources of estimated Mach number interpolation error than the boattail expansions/shocks and plume shock diamonds.

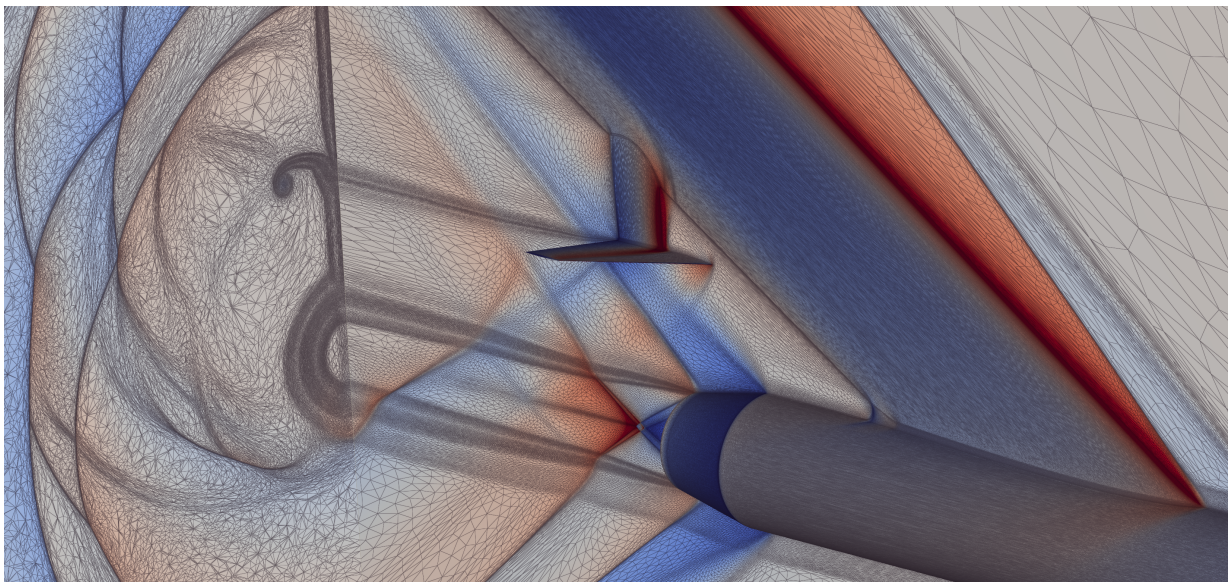
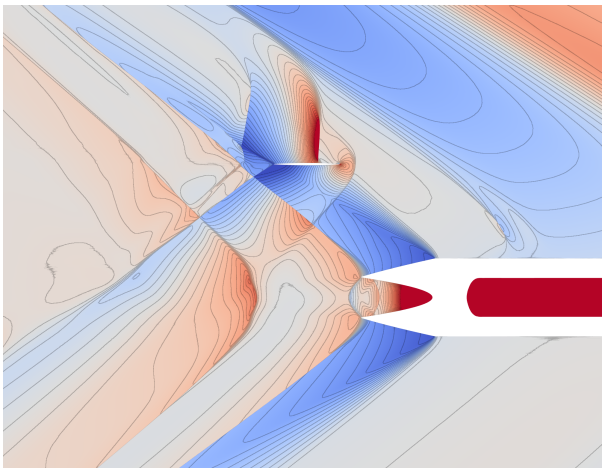
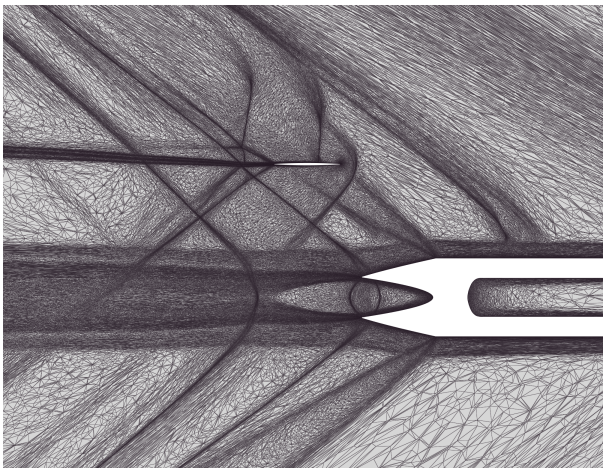


Fig. 2 Biconvex solution obtained with Wolf and L^4-norm Mach interpolation error control, 26.3M vertices (156M tetrahedra).

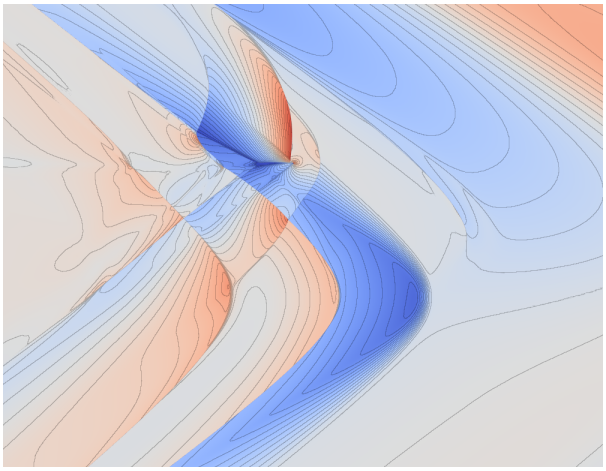
Figure 3 shows complex 3D shock-boundary layer and shock-plume interaction with a series of y-constant planes. These biconvex solutions are obtained with Wolf on the finest grid with L^4-norm Mach interpolation error control. These meshes contain 26.3M vertices and 156M tetrahedra and the intersection of the tetrahedra with the plane is shown. The pressure ratio $\Delta p/p_\infty$ is shown on different plane cuts with a normal along the y-axis. The range of the colormap for the pressure ratio is uniform from $\Delta p/p_\infty = -0.4$ [−] (blue) to $\Delta p/p_\infty = +0.4$ [−] (red). The gray color represents a zero pressure ratio. The boundary layer and wake of the interior and exterior of the model are seen in Fig. 3b. The geometric source of shocks and expansions can be traced and plume shock diamonds observed in this figure. Complex shock and expansion interaction is seen in the remaining subfigures.



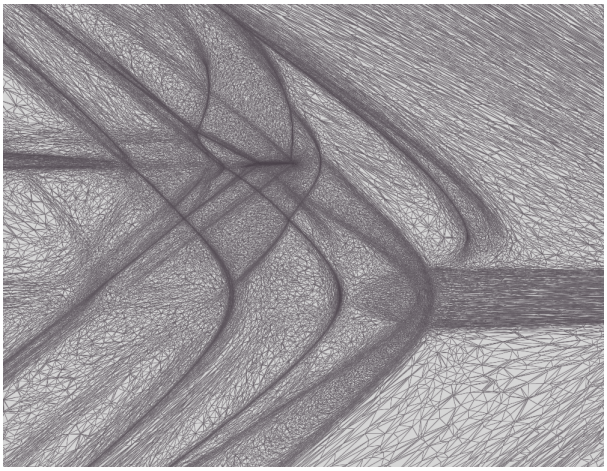
(a) Pressure ratio at $y = 0.45$ $[in]$**.**



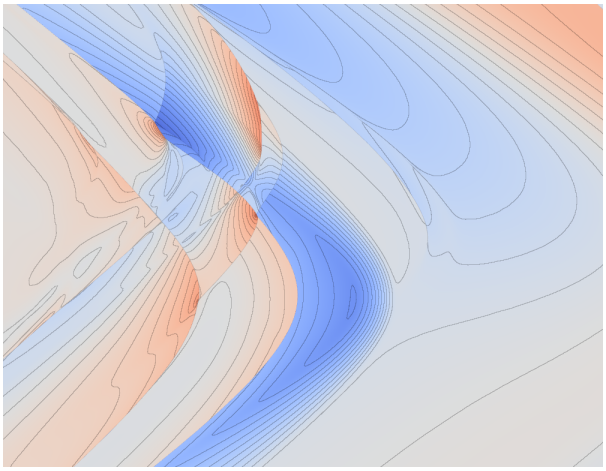
(b) Mesh at $y = 0.45$ $[in]$**.**



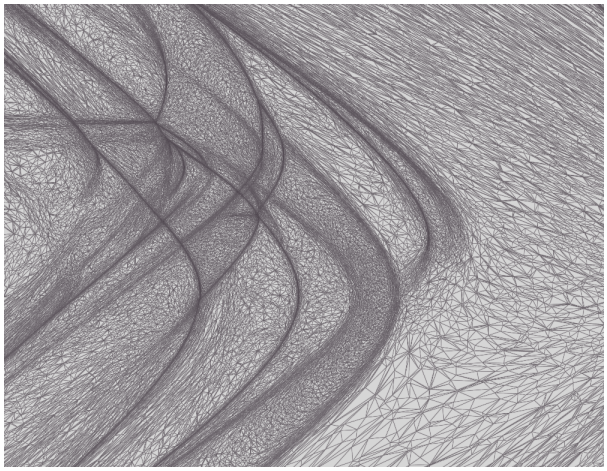
(c) Pressure ratio at $y = 0.90$ $[in]$**.**



(d) Mesh at $y = 0.90$ $[in]$**.**



(e) Pressure ratio at $y = 1.35$ $[in]$**.**



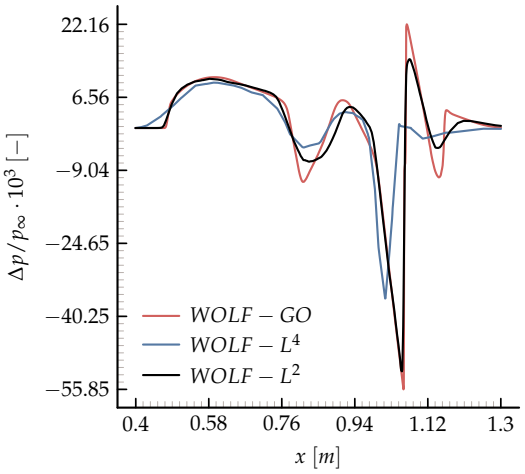
(f) Mesh at $y = 1.35$ $[in]$**.**

Fig. 3 Biconvex pressure ratio and tetrahedra intersected with y-constant plane.

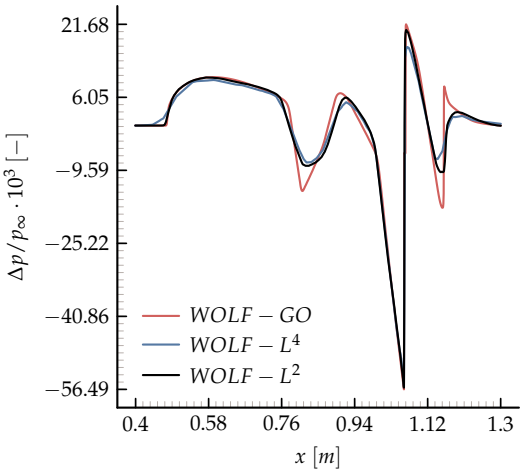
Figures 4, 5 and 6 show increasing mesh refinement (complexity) at different angles of $\varphi = 0°$, $\varphi = 15°$ and $\varphi = 30°$, respectively, for WOLF with `Feflo.a`. The metric formulations are pressure signature goal-oriented (GO), L^4-norm Mach interpolation error (L^4), and L^2-norm Mach interpolation error (L^2). All the three approaches converge to the

same gross signature. However, the goal-oriented metric produces more accurate signatures on a coarse mesh (i.e., the structure is well captured with the smallest complexity of 0.2M).

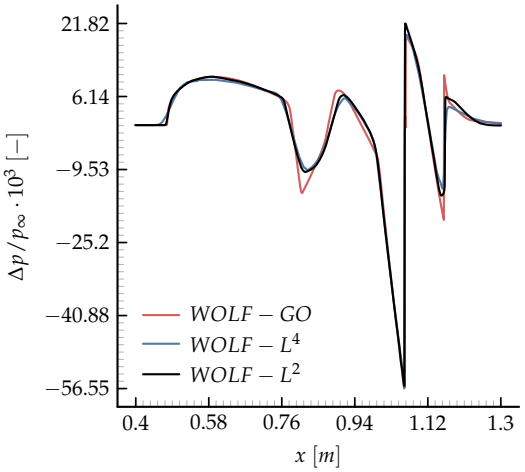
The cone forebody signature extends to $x = 0.76\ [m]$, where the expansion steepens as the body transitions from a cone to a cylinder. A compression centered at $x = 0.86\ [m]$ is due to the blade sting leading-edge shock wrapping around the cylindrical body. The boattail creates the strongest expansion starting at $x = 1.00\ [m]$ and the nozzle lip creates the strongest shock at $x = 1.06\ [m]$. The N-shaped shock structure is the first plume shock diamond and it contains the much weaker biconvex shock generator signature. The finest goal-oriented mesh resolves very fine details of the key shock-plume interaction not resolved by the interpolation-error control.



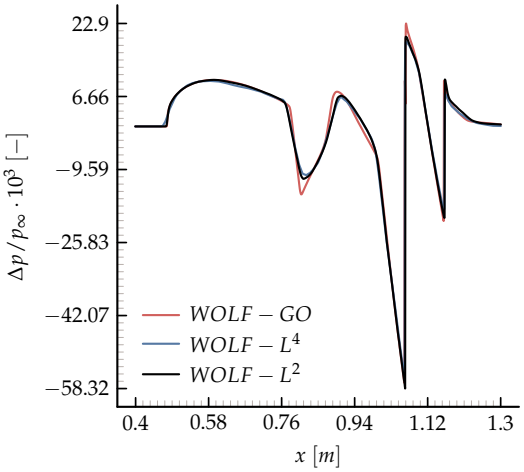
(a) Complexity of 0.2**M.**



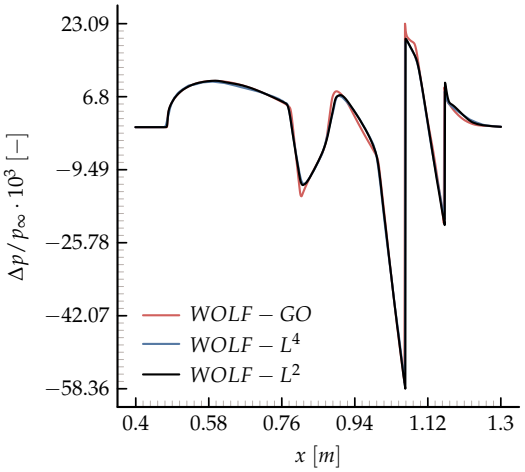
(b) Complexity of 0.4**M.**



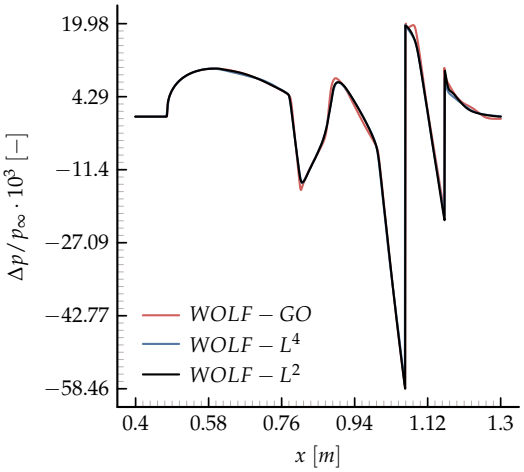
(c) Complexity of 0.8**M.**



(d) Complexity of 1.6**M.**

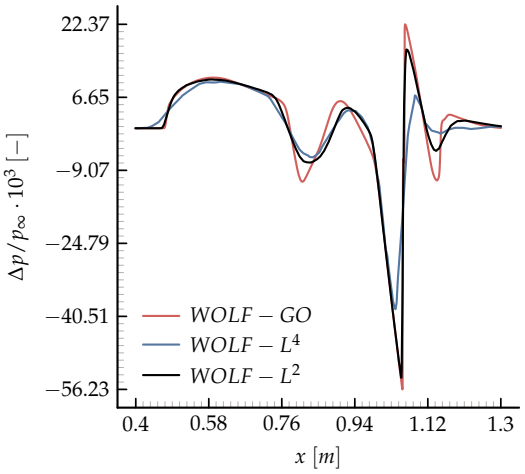


(e) Complexity of 3.2**M.**

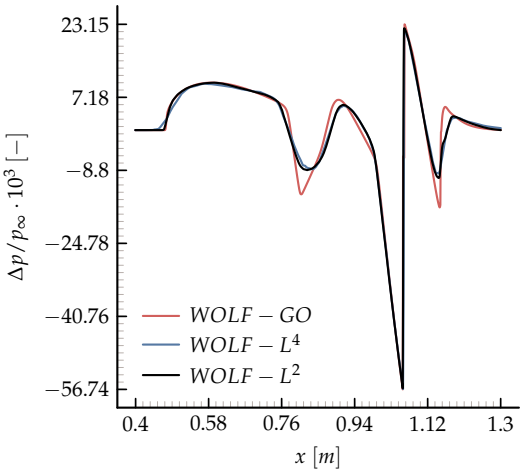


(f) Complexity of 6.4**M.**

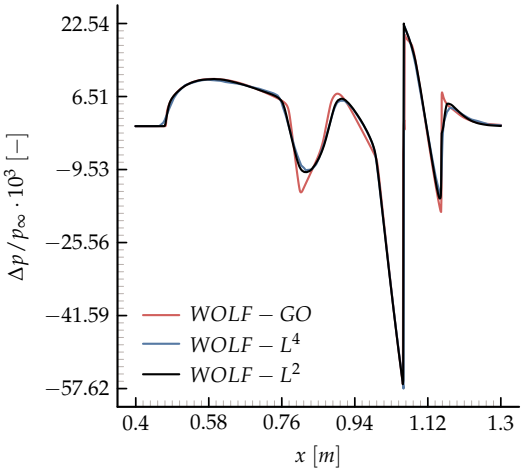
Fig. 4 Pressure signature at $\varphi = 0°$ for the three different metric formulations with WOLF.



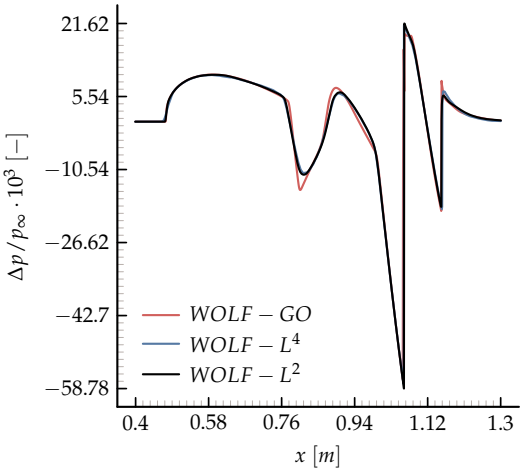
(a) Complexity of 0.2M.



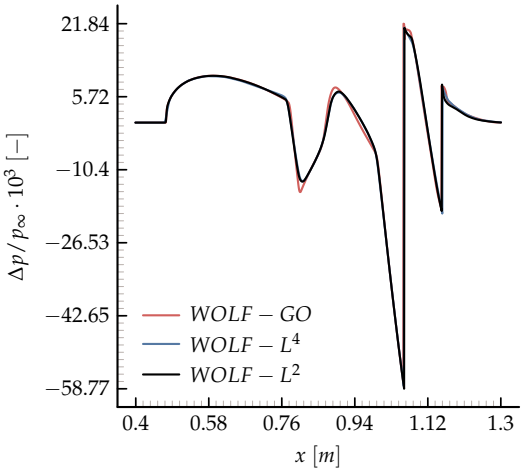
(b) Complexity of 0.4M.



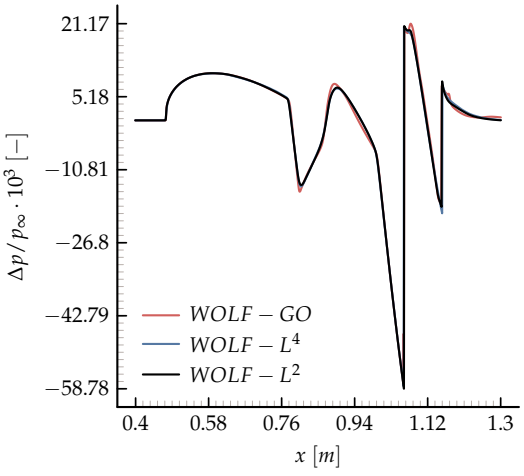
(c) Complexity of 800k.



(d) Complexity of 1.6M.

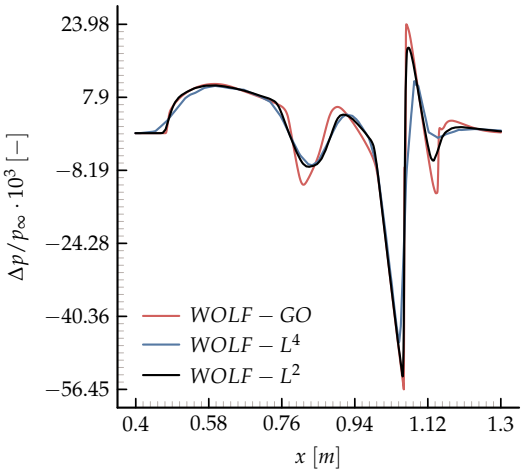


(e) Complexity of 3.2M.

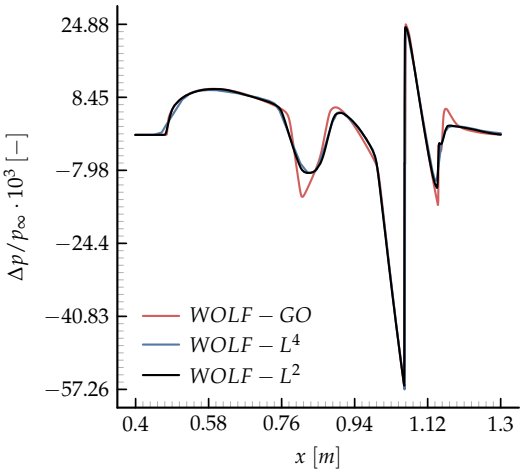


(f) Complexity of 6.4M.

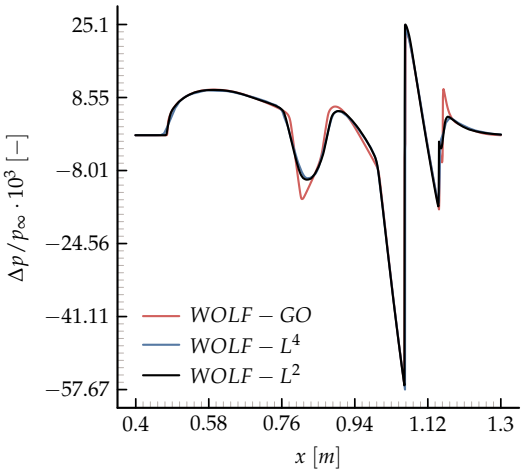
Fig. 5 Pressure signature at $\varphi = 15°$ for the three different metric formulations with WOLF.



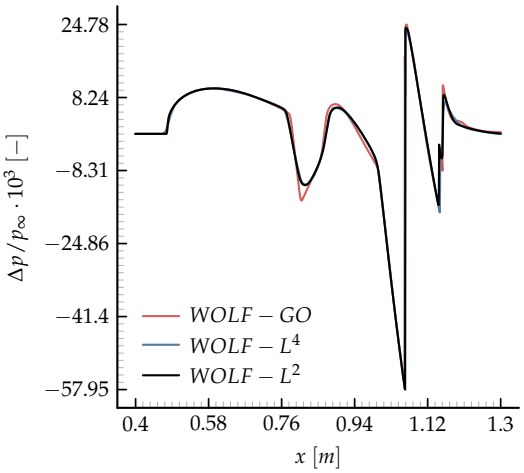
(a) Complexity of 0.2**M.**



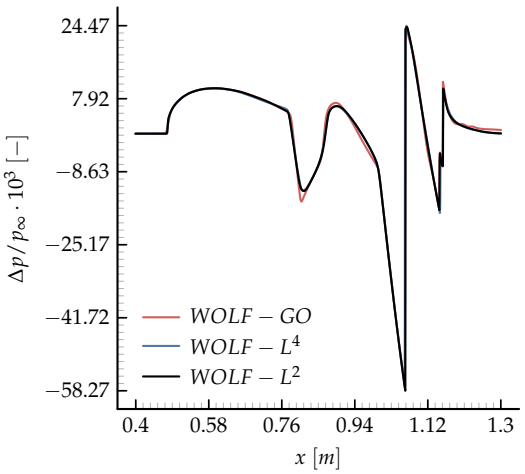
(b) Complexity of 0.4**M.**



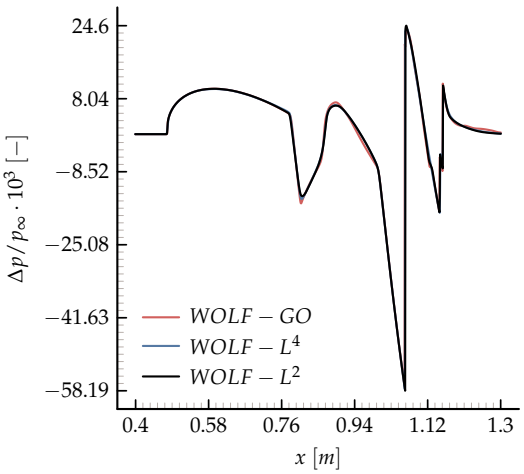
(c) Complexity of 0.8**M.**



(d) Complexity of 1.6**M.**



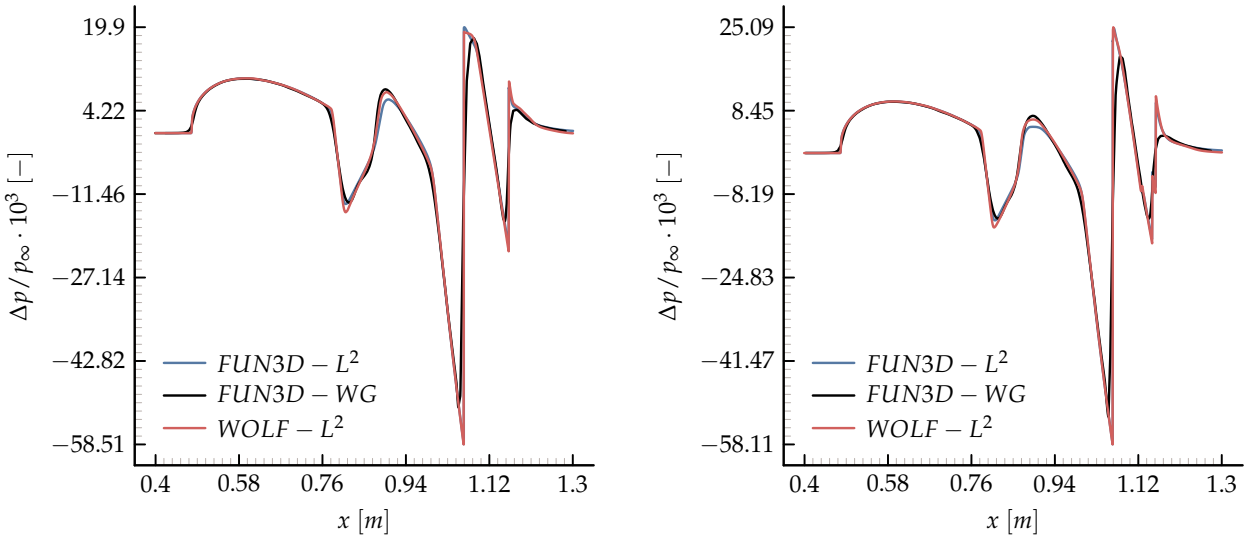
(e) Complexity of 3.2**M.**



(f) Complexity of 6.4**M.**

Fig. 6 Pressure signature at $\varphi = 30°$ for the three different metric formulations with WOLF.

Pressure signatures for two different angles obtained by three different methods are shown in Fig. 7. The FUN3D-FV results are obtained with L^2-norm interpolation control and the finest workshop-provided mesh (WG) [41]. The last signature is obtained on adapted grids with WOLF L^2-norm interpolation control. The workshop-provided mesh results are underresolved as compared to the adaptive results. With the exception of the model support sting shock, $x = 0.90\,[m]$, the two adaptive methods overplot. This favorable agreement between the adaptive-mesh methods includes the key shock-plume interaction region. Repeatable results with independent implementations may indicate that solution mesh and solver independence is possible with adaptive-mesh methods.



(a) $\varphi = 0°$. **(b)** $\varphi = 30°$.

Fig. 7 Adapted and workshop-provided signatures for FUN3D-FV and WOLF.

The biconvex wind tunnel test included Retroreflective Background Oriented Schlieren (RBOS) imaging [42]. FUN3D-FV computational schlieren [43] is computed and inset into an RBOS image, Fig. 8. The shock and plume structures observed in the wind tunnel test are captured by the computational schlieren, but some features are slightly displaced due to small local Mach number and local flow direction variations between the simulation and experiment. This technique of observed and simulated image comparison provides a unique tool for method validation and provides context for the computed solution details observed in the signatures, meshes, and pressure fields.

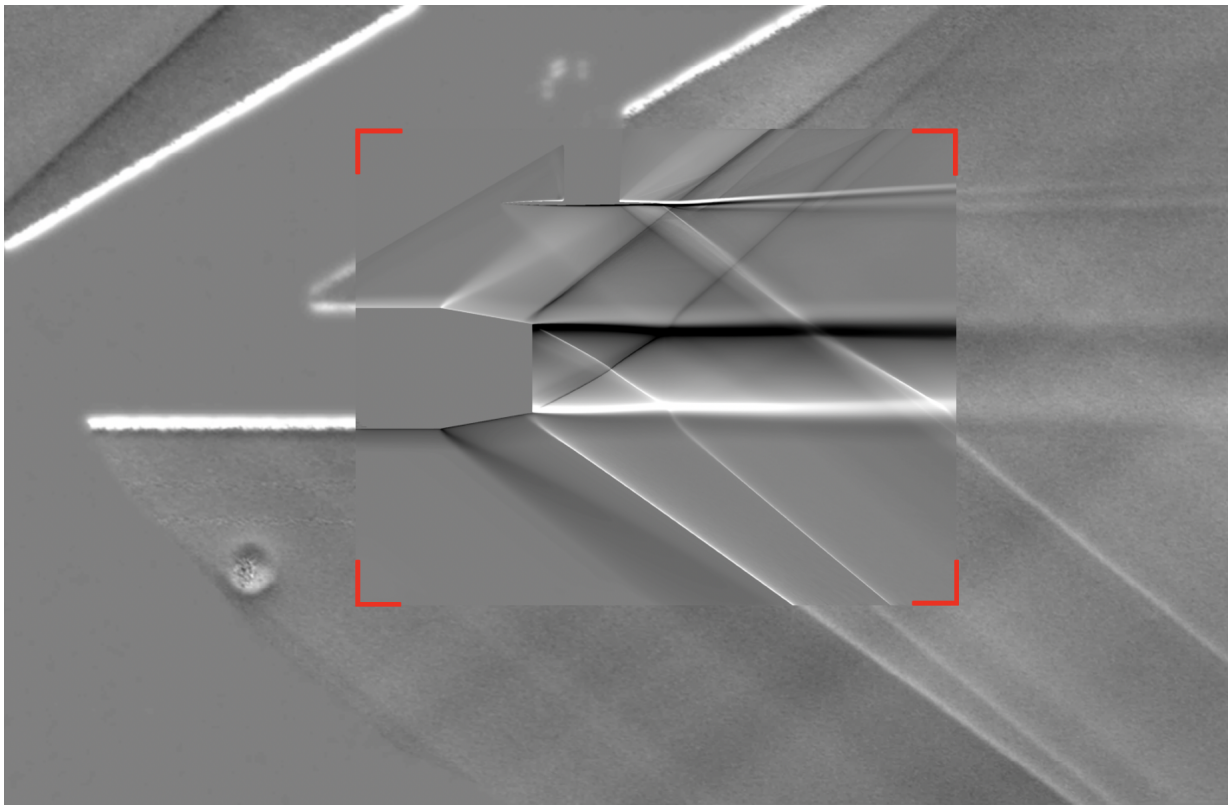


Fig. 8 Computational schlieren inset into an RBOS image showing shock and plume structure of the biconvex.

B. C608 Low-Boom Flight Demonstrator

Figure 9 shows the geometry of the C608 Low-Boom Flight Demonstrator. All the computations are carried out with the physical parameters and nondimensional boundary conditions listed in Table 2 with the U.S. standard atmosphere (1976).

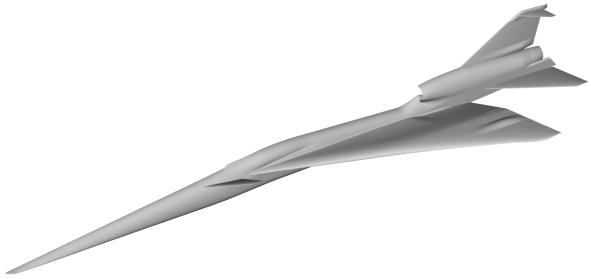


Fig. 9 C608 Low-Boom Flight Demonstrator geometry.

Table 2 C608 Low-Boom Flight Demonstrator simulation conditions.

Characteristic	Symbol	Value	Units
Mach	M	1.4	$[-]$
Angle of attack	α	0.0	$[-]$
Body length	L	1080	$[in]$
Altitude	H	53200	$[ft]$

Temperature	T	389.9	$[R]$
Unit Reynolds number (per inch)	Re	109776	$[-]$
Static pressure to freestream ratio at an engine fan face		2.6	$[-]$
Static pressure to freestream ratio at Environmental Control System (ECS) inlet face		1.4	$[-]$
Engine plenum total pressure ratio to freestream static pressure		10.0	$[-]$
Engine plenum total temperature ratio to freestream static temperature		7.0	$[-]$
Bypass total pressure ratio to freestream static pressure		2.4	$[-]$
Bypass plenum total temperature ratio to freestream static temperature		2.0	$[-]$

The mesh-adapted Wolf and FUN3D-FV solutions used control of L^2-norm Mach interpolation error. FUN3D-FV signatures on the workshop-provided meshes are also included. For Wolf, a series of increasing complexities [0.8M, 1.6M, 3.2M, 6.4M, 12.8M] is used to create 25 meshes. For each complexity, five meshes are generated to ensure the convergence of the mesh and metric. The final mesh is composed of 26.4M vertices and 156M tetrahedra for Wolf.

Figure 10 shows the propagation of all the shock waves around the aircraft as well as the aircraft wake. This Wolf adapted mesh and solution are composed of 26.4M vertices and 156M tetrahedra. The pressure ratio $\Delta p/p_\infty$ is shown on the symmetry plane, on the aircraft skin and on a plane cut with a normal along the x-axis with the mesh. The range of the colormap for the pressure ratio is uniform from $\Delta p/p_\infty = -0.12$ $[-]$ (blue) to $\Delta p/p_\infty = +0.12$ $[-]$ (red). The gray color represents a zero pressure ratio. The extremely complex 3D shock and expansion patterns of the C608 nearfield are evident on the x-constant intersection plane. This complex shock-expansion-wake interaction must be accurately captured to realize the low-boom character of the extracted nearfield signature.

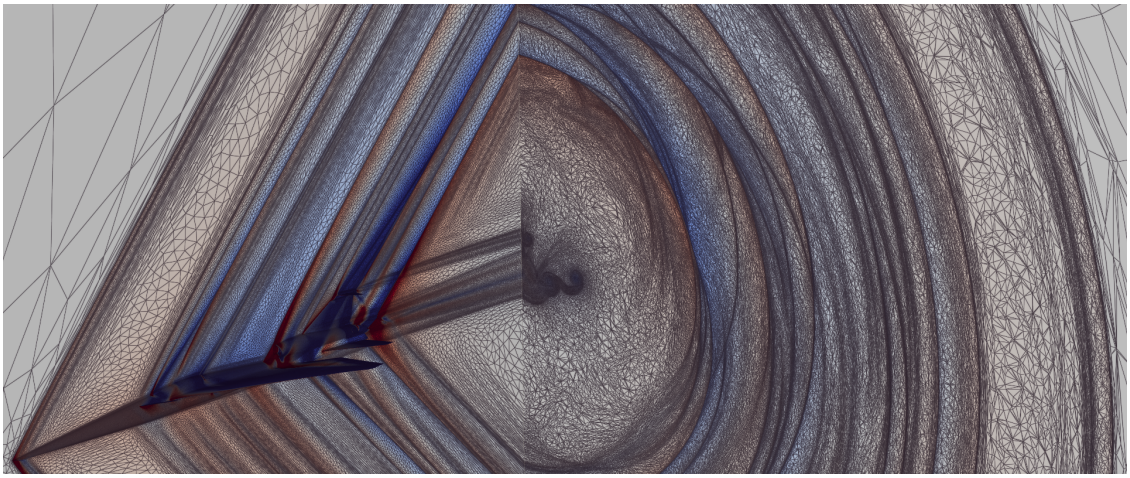
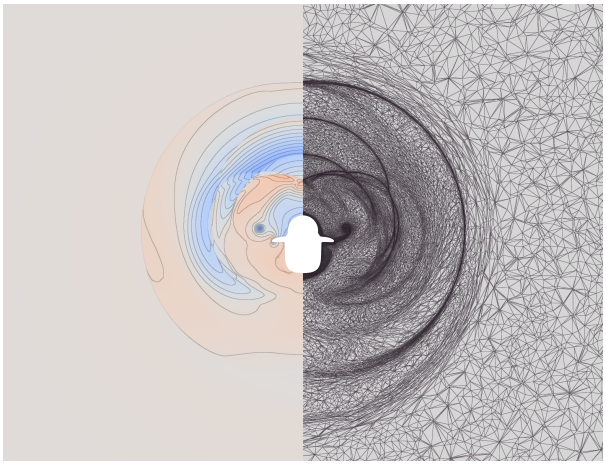
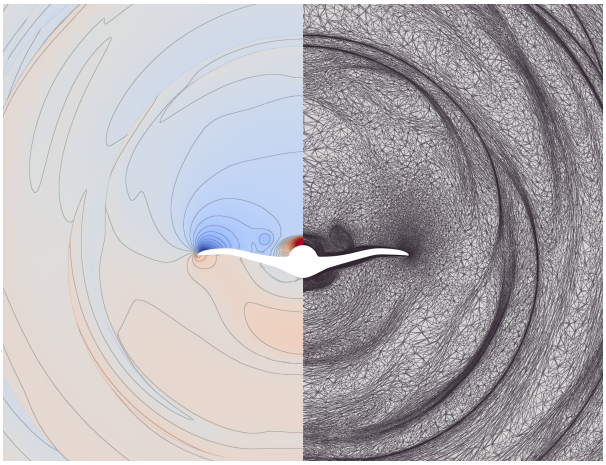


Fig. 10 C608 Low-Boom Flight Demonstrator solution obtained with Wolf on the finest L^2-norm adapted mesh.

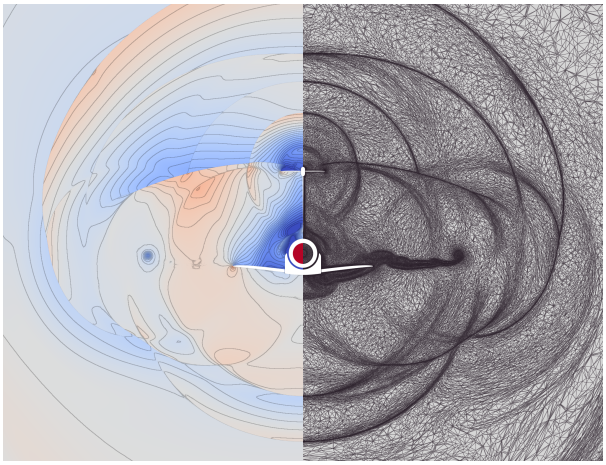
Figure 11 shows the intersection of the tetrahedra with x-constant planes. This Wolf adapted mesh and solution are composed of 26.4M vertices and 156M tetrahedra. The pressure ratio $\Delta p/p_\infty$ on different plane cuts with a normal along the x-axis is shown. The range of the colormap for the pressure ratio is uniform from $\Delta p/p_\infty = -0.3$ $[-]$ (blue) to $\Delta p/p_\infty = +0.3$ $[-]$ (red). The gray color represents a zero pressure ratio. This series of x-constant intersection planes shows the generation, evolution, and complex interaction of boundary layers, wake, plume, vortices, shocks, and expansions. The sonic boom tailoring of the nearfield pressures both near the centerline and 45° offtrack provide a quiet primary sonic boom carpet.



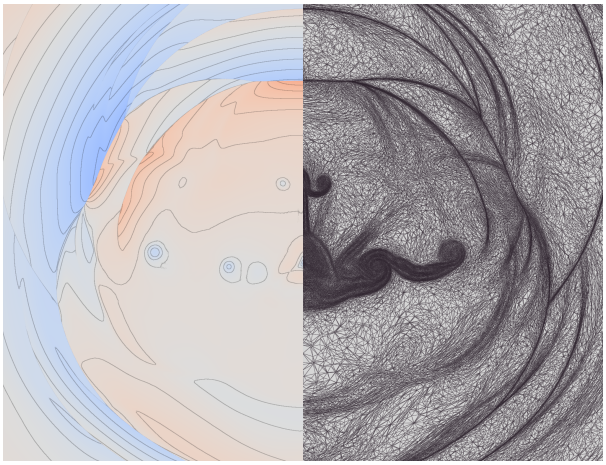
(a) $x/L = 0.50$ [−].



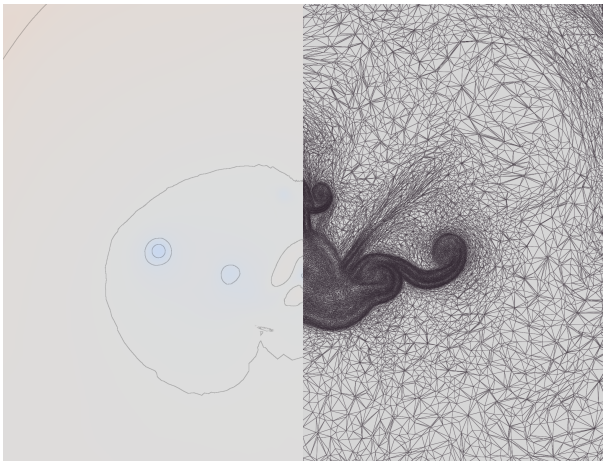
(b) $x/L = 0.75$ [−].



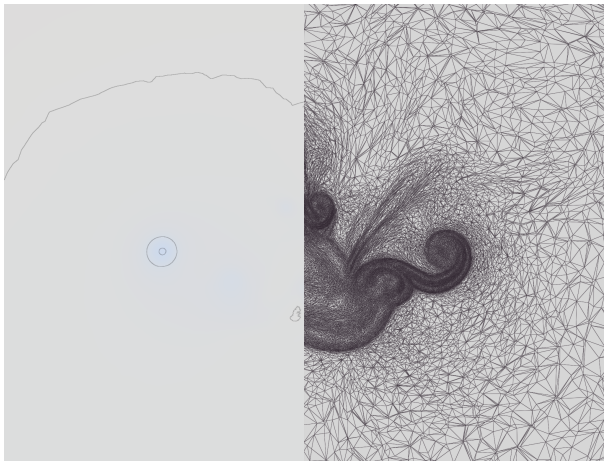
(c) $x/L = 1.00$ [−].



(d) $x/L = 1.25$ [−].



(e) $x/L = 1.50$ [−].

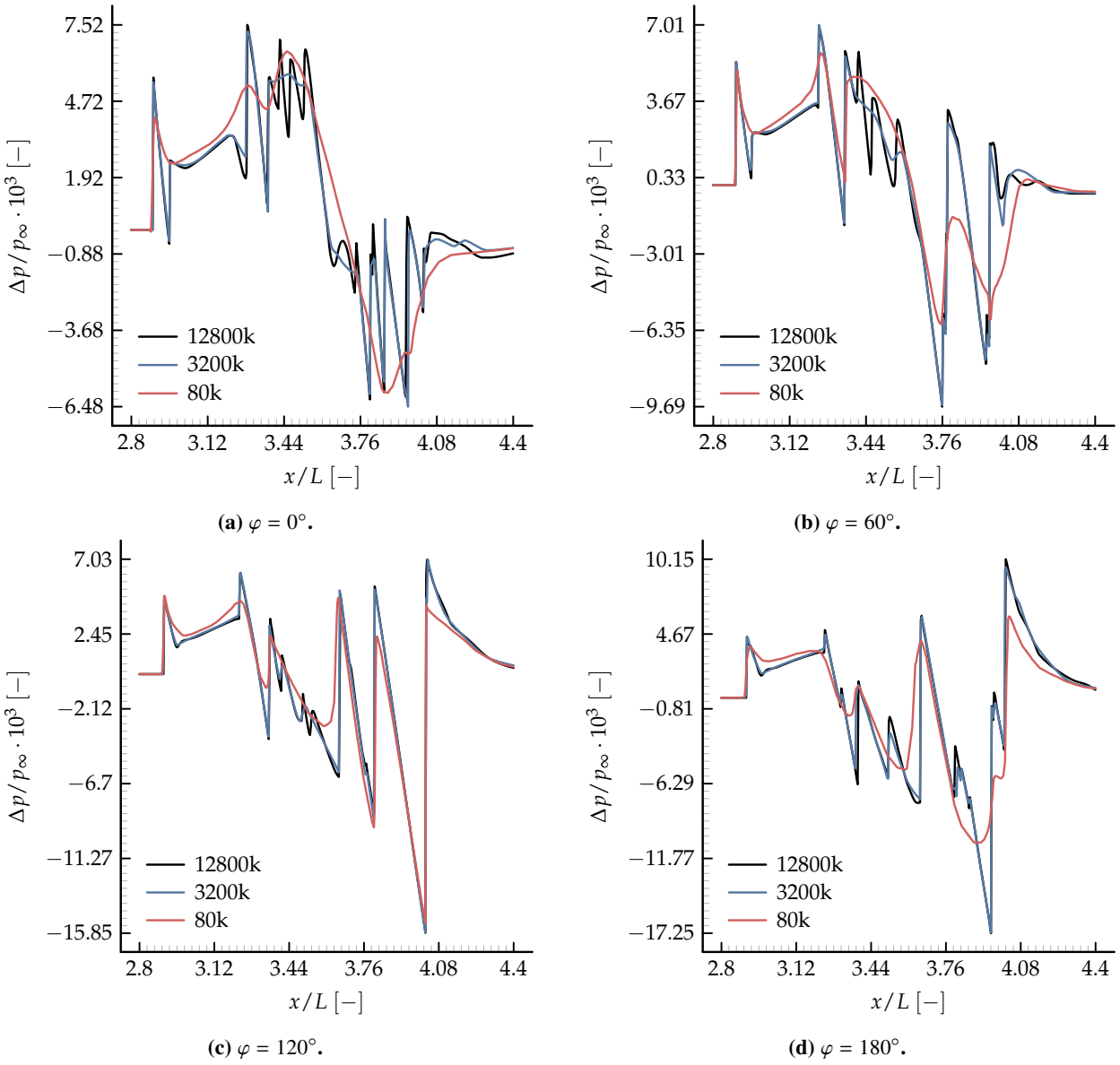


(f) $x/L = 1.75$ [−].

Fig. 11 C608 Low-Boom Flight Demonstrator mesh and solution obtained with WOLF L^2 metric intersected with x-constant planes

The pressure ratio $(p - p_\infty)/p_\infty = \Delta p/p_\infty$ is extracted on a cylinder of a radius $R = 3240$ $[in]$ along the x-axis between an angle from 0° to 180° with a step of 2°. Figure 12 shows the impact of mesh resolution on nearfield pressure singature for different angles of extraction. The pressure signature scale at $\varphi = 0°$ (pointing toward the ground) is

much lower than the pressure scale at $\varphi = 180°$ (pointing upward). The nose creates an N-wave that is followed by a compression as the area of the slender nose increases to the canard. The complex series of shocks is due to the canard, canopy, wing leading edge, and ECS inlet. The wing creates an expansion. The complex series of shocks in the aft portion of the signature is due to the wing trailing edge, empennage, and plume. The mitigation of the nearfield pressure signature under the vehicle indicates the outstanding design effort invested in this demonstrator, which lowers the impact of the shock waves on the ground.

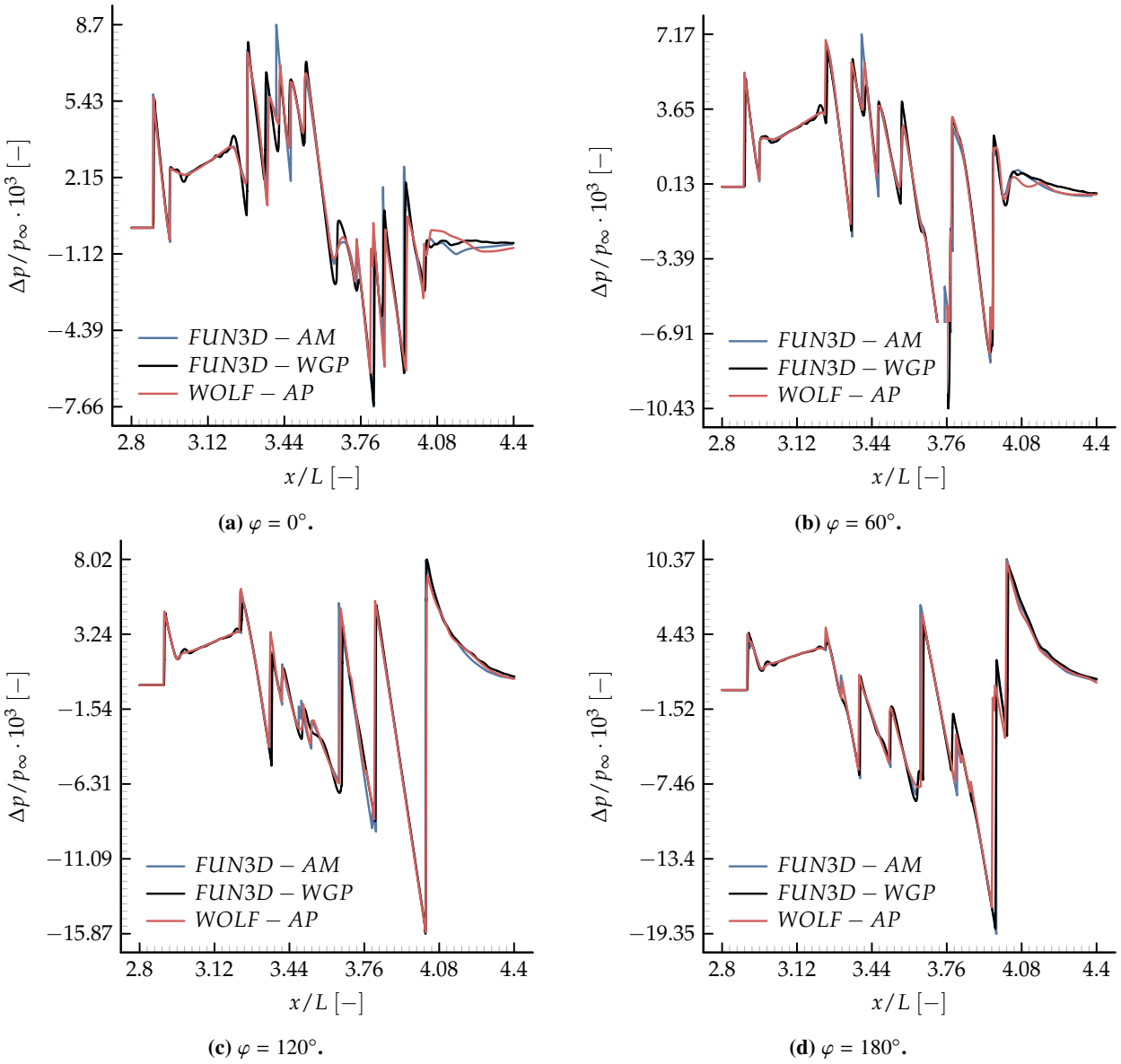


(a) $\varphi = 0°$. **(b)** $\varphi = 60°$.

(c) $\varphi = 120°$. **(d)** $\varphi = 180°$.

Fig. 12 Mesh convergence on the pressure signature for different angles obtained with Wolf L^2 metric.

In Fig. 13, WOLF-AP stands for Wolf L^2 Adapted Pressure boundary condition, FUN3D-AM stands for FUN3D-FV L^2 Adapted Mach boundary condition, and FUN3D-WGP stands for FUN3D-FV Workshop Grids Pressure boundary condition. There is good agreement between methods. The differences in Environmental Control System (ECS) boundary conditions are seen at $x/L = 3.4\,[-]$ in Fig. 13a. There are some differences seen in the challenging plume region $x/L > 4.0\,[-]$ and the extremely sensitive shock location at $x/L = 3.0\,[-]$. The nearfield pressure agreement is similar below, beside, and above the configuration.

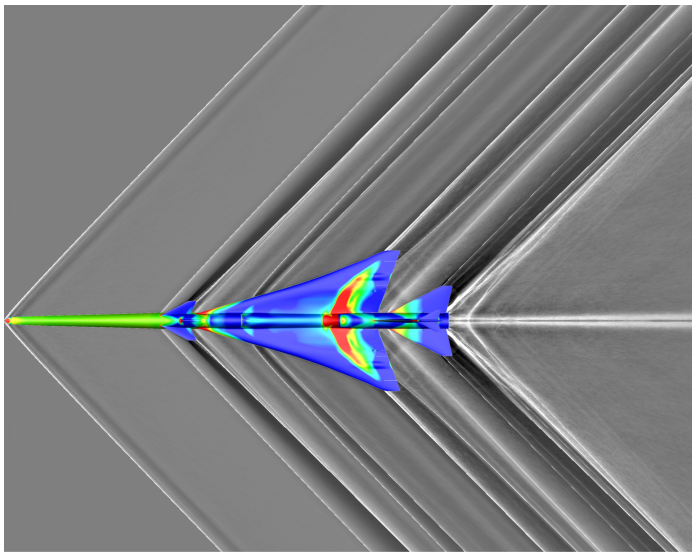


(a) $\varphi = 0°$. **(b)** $\varphi = 60°$.

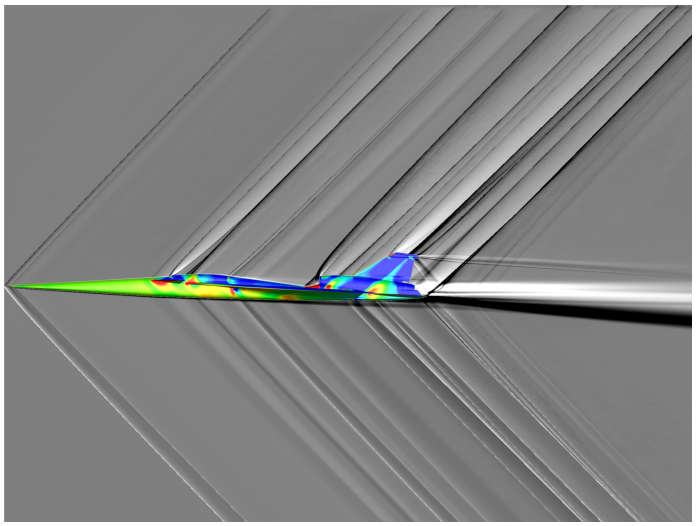
(c) $\varphi = 120°$. **(d)** $\varphi = 180°$.

Fig. 13 Pressure signature for different angles obtained by three different methods.

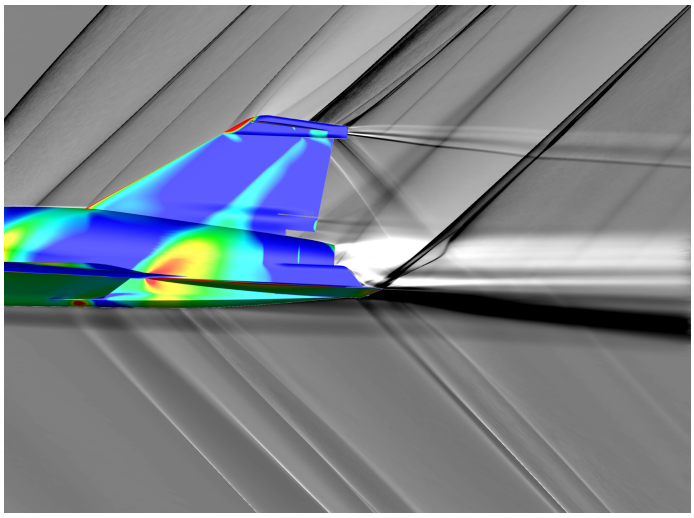
FUN3D-FV computational schlieren is shown in Fig. 14 for the finest L^2-norm Mach interpolation control mesh. The boundary layer, shock, plume, wake, and vortex structures are observed in these computational schlieren images. These flow features are also seen in the adapted mesh and solution, Figs. 10 and 11. The interaction of these flow features is particularly intense in the tail and near-plume regions. The signatures at different angles in Figs. 12 and 13 show the stronger shocks to the side and above the configuration, which is also observed in Fig. 14. This computational approach would allow for comparison with future in-flight observations [44] to form an improved understanding of the Low-Boom Flight Demonstrator nearfield.



(a) Top-down view.



(b) Side view.

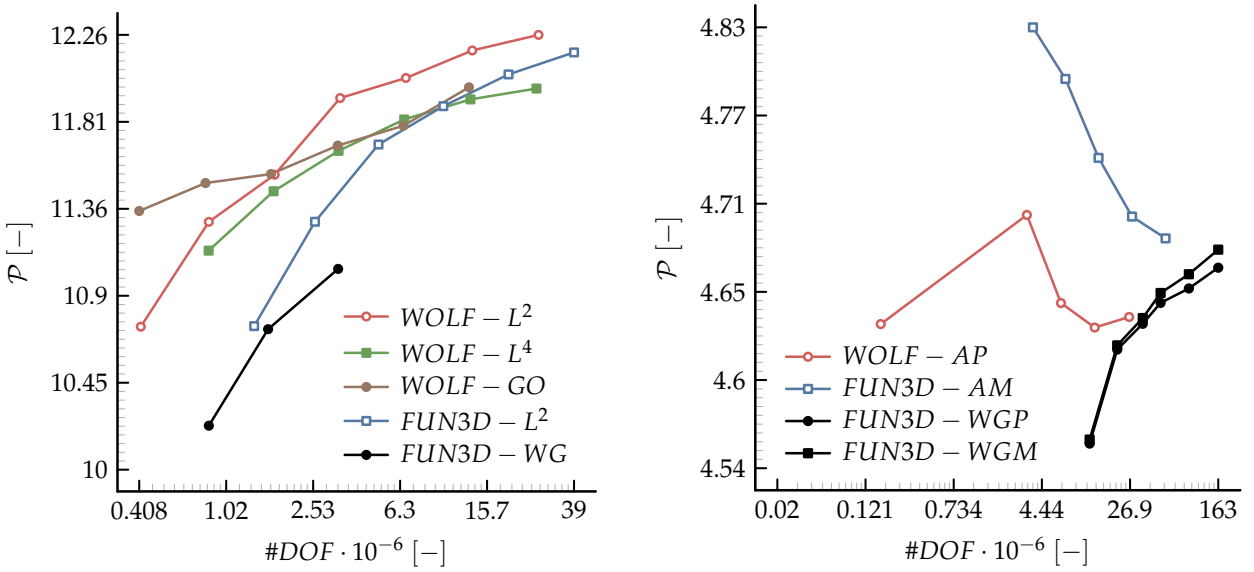


(c) Side view (zoom).

Fig. 14 C608 FUN3D-FV computational schlieren with surface pressure.

C. Nearfield Pressure Integral Convergence

The mesh convergence of integrals of the pressure signatures are shown in Fig. 15. The quantity $\mathcal{P}$ in Fig. 15a is the mean of the L^2-norm of the pressure ratio at $\varphi = 0°$, $\varphi = 15°$ and $\varphi = 30°$. The L^2 Mach interpolation error control for both FUN3D-FV and Wolf appear to be converging with the Wolf goal-oriented trajectory. The workshop mesh series is too coarse to determine if FUN3D-FV with fixed meshes will approach the finer adapted meshes. The L^2 Mach interpolation error control with Wolf appears to be approaching a lower value, which may be due to the L^4-norm placing more emphasis on the nonsmooth regions where the GO and L^2-norm balances smooth (boundary layers and expansions) and nonsmooth (shocks) features.



(a) Mesh convergence of the biconvex 9×7 test case for the three different approaches.

(b) Mesh convergence of C608 Low-Boom Flight Demonstrator test case.

Fig. 15 Mesh convergence of SBPW3 nearfield signature integrals.

Figure 15b shows the convergence of the quantity $\mathcal{P}$ which is the mean of the L^2-norm of the pressure ratio for $\varphi = 0°$ to $\varphi = 180°$ with a step of $2°$. AP is the L^2-norm Mach interpolation error control with pressure-based inlet boundary conditions. AM is the L^2-norm Mach interpolation error control with Mach-based inlet boundary conditions. WGP and WGM are workshop meshes with pressure-based and Mach-based inlet boundary conditions. These multiple methods may approach the same values for each set of boundary conditions, but these trajectories are difficult to predict without finer adapted meshes.

VI. Conclusion

Anisotropic adaptive-mesh strategies were applied to the complex geometries of the Third AIAA Sonic Boom Workshop. These configurations presented important propulsion interaction effects that were resolved to obtain accurate nearfield sonic boom signatures. Anisotropic metrics were formulated to control estimated Mach interpolation error and estimated integrated nearfield pressure signature (goal-oriented) error. Adapted meshes constructed with multiple iterations of flow (and adjoint) solves, metric construction, and metric conforming mesh adaptation were used to construct geometry constrained meshes that resolved the key boundary layer, shock, plume, wake, and vortex structures. The complex interaction of these key features was also captured and depicted in intersection planes and computational schlieren. As seen in previous sonic boom workshops, the difficulty (and variation between methods) was largest in the aft portion of the nearfield signatures where these key flow features interact and small upstream solution errors accumulate.

Results on these adapted meshes were compared with the results obtained on workshop-provided, fixed meshes. Small details of the shock generator and plume nearfield signature were seen in the adapted meshes, but absent in the fixed-meshes. Obtaining these subtle details of the shock-plume interaction experiment are indicators that the adapted

meshes were suitable for resolving the flow-feature interaction effects critical to accurate nearfield prediction. The favorable comparison of independent implementations of the entire simulation process provided evidence that each process was implemented correctly, which set a solid foundation for confidence in the nearfield prediction of each method. These comparisons also provided evidence that mesh and solver independent solutions were possible with solution-adaptive methods.

Detailed flow solutions and mesh renderings were combined with computational schlieren images to reveal the complex interactions present in a shock-plume interaction wind tunnel model and a prototype of the Low-Boom Flight Demonstrator. Accurate prediction and understanding of these key flow feature interactions in the nearfield is critical for the analysis and development of low-boom supersonic aircraft. The convergence of the integral of the nearfield signature with increasing mesh resolution was shown for multiple metric formulations, two flow solvers, and a series of refined workshop-provided meshes. Demonstrating reliable nearfield sonic boom prediction through these methods is critical to encouraging an examination of the overland commercial supersonic ban and supporting the creation of a certification standard to replace the ban.

Acknowledgments

Neal Smith (AerospaceComputing, Inc./NASA Ames Research Center) provided the RBOS image for the biconvex 9×7 wind tunnel campaign [42]. This work is partially supported under by NASA Fundamental Aerodynamics by Commercial Supersonic Transport (CST) and Transformational Tools and Technologies (TTT) programs.

References

[1] Balan, A., Park, M. A., Anderson, W. K., Kamenetskiy, D. S., Krakos, J. A., Michal, T., and Alauzet, F., "Verification of Anisotropic Mesh Adaptation for RANS Simulations over ONERA M6 Wing," *AIAA Journal*, Vol. 58, No. 4, 2020, pp. 1550–1565. https://doi.org/10.2514/1.J059158.

[2] Galbraith, M. C., Caplan, P. C., Carson, H. A., Park, M. A., Balan, A., Anderson, W. K., Michal, T., Krakos, J. A., Kamenetskiy, D. S., Loseille, A., Alauzet, F., Frazza, L., and Barral, N., "Verification of Unstructured Grid Adaptation Components," *AIAA Journal*, Vol. 58, No. 9, 2020, pp. 3947–3962. https://doi.org/10.2514/1.J058783.

[3] Park, M. A., Kleb, B., Jones, W. T., Krakos, J. A., Michal, T., Loseille, A., Haimes, R., and Dannenhoffer, J. F., III, "Geometry Modeling for Unstructured Mesh Adaptation," AIAA Paper 2019–2946, 2019.

[4] Michal, T., Krakos, J., Kamenetskiy, D., Galbraith, M., Ursachi, C.-I., Park, M. A., Anderson, W. K., Alauzet, F., and Loseille, A., "Comparing Unstructured Adaptive Mesh Solutions for the High Lift Common Research Model Airfoil," AIAA Paper 2020–3219, 2020.

[5] Alauzet, F., and Loseille, A., "A Decade of Progress on Anisotropic Mesh Adaptation for Computational Fluid Dynamics," *Computer-Aided Design*, Vol. 72, 2016, pp. 13–39. 23rd International Meshing Roundtable Special Issue: Advances in Mesh Generation, https://doi.org/10.1016/j.cad.2015.09.005.

[6] Alauzet, F., and Loseille, A., "High-Order Sonic Boom Modeling Based on Adaptive Methods," *Journal of Computational Physics*, Vol. 229, No. 3, 2010, pp. 561–593. https://doi.org/10.1016/j.jcp.2009.09.020.

[7] Loseille, A., Frazza, L., and Alauzet, F., "Comparing Anisotropic Adaptive Strategies on the 2nd AIAA Sonic Boom Workshop Geometry," *AIAA Journal of Aircraft*, Vol. 56, No. 3, 2019, pp. 938–952. https://doi.org/10.2514/1.C034840.

[8] Batten, P., Clarke, N., Lambert, C., and Causon, D. M., "On the Choice of Wavespeeds for the HLLC Riemann Solver," *SIAM Journal on Scientific Computing*, Vol. 18, No. 6, 1997, pp. 1553–1570. https://doi.org/10.1137/S1064827593260140.

[9] Spalart, P. R., and Allmaras, S. R., "A One-Equation Turbulence Model for Aerodynamic Flows," *La Recherche Aérospatiale*, Vol. 1, 1994, pp. 5–21.

[10] Menier, V., Loseille, A., and Alauzet, F., "CFD Validation and Adaptivity for Viscous Flow Simulations," AIAA Paper 2014–2925, 2014.

[11] Pandya, M. J., Diskin, B., Thomas, J. L., and Frink, N. T., "Improved Convergence and Robustness of USM3D Solutions on Mixed-Element Grids," *AIAA Journal*, Vol. 54, No. 9, 2016, pp. 2589–2610. https://doi.org/10.2514/3.12701.

[12] Saad, Y., and Schultz, M. H., "GMRES: A Generalized Minimum Residual Algorithm for Solving Nonsymmetric Linear Systems," *SIAM Journal of Scientific and Statistical Computing*, Vol. 7, 1986, pp. 856–869.

[13] Anderson, W. K., and Bonhaus, D. L., "An Implicit Upwind Algorithm for Computing Turbulent Flows on Unstructured Grids," *Computers and Fluids*, Vol. 23, No. 1, 1994, pp. 1–22. https://doi.org/10.1016/0045-7930(94)90023-X.

[14] Biedron, R. T., Carlson, J.-R., Derlaga, J. M., Gnoffo, P. A., Hammond, D. P., Jones, W. T., Kleb, B., Lee-Rausch, E. M., Nielsen, E. J., Park, M. A., Rumsey, C. L., Thomas, J. L., Thompson, K. B., and Wood, W. A., "FUN3D Manual: 13.6," NASA TM-2019-220416, Langley Research Center, Oct. 2019. https://doi.org/2060/20190033239.

[15] Roe, P. L., "Approximate Riemann Solvers, Parameter Vectors, and Difference Schemes," *Journal of Computational Physics*, Vol. 43, No. 2, 1981, pp. 357–372. https://doi.org/10.1016/0021-9991(81)90128-5.

[16] van Leer, B., "Towards the Ultimate Conservative Difference Scheme. II. Monotonicity and Conservation Combined in a Second-Order Scheme," *Journal of Computational Physics*, Vol. 14, No. 4, 1974, pp. 361–370. https://doi.org/10.1016/0021-9991(74)90019-9.

[17] Nielsen, E. J., Lu, J. C.-C., Park, M. A., and Darmofal, D. L., "An Implicit, Exact Dual Adjoint Solution Method for Turbulent Flows on Unstructured Grids," *Computers and Fluids*, Vol. 33, No. 9, 2004, pp. 1131–1155. https://doi.org/10.1016/j.compfluid.2003.09.005.

[18] Bonet, J., and Peraire, J., "An Alternating Digital Tree (ADT) Algorithm for 3D Geometric Searching and Intersection Problems," *International Journal for Numerical Methods in Engineering*, Vol. 31, No. 1, 1991, pp. 1–17. https://doi.org/10.1002/nme.1620310102.

[19] Loseille, A., and Alauzet, F., "Continuous Mesh Framework Part I: Well-Posed Continuous Interpolation Error," *SIAM Journal on Numerical Analysis*, Vol. 49, No. 1, 2011, pp. 38–60. https://doi.org/10.1137/090754078.

[20] Loseille, A., and Alauzet, F., "Continuous Mesh Framework Part II: Validations and Applications," *SIAM Journal on Numerical Analysis*, Vol. 49, No. 1, 2011, pp. 61–86. https://doi.org/10.1137/10078654X.

[21] Loseille, A., and Alauzet, F., "Optimal 3D Highly Anisotropic Mesh Adaptation Based on the Continuous Mesh Framework," *Proceedings of the 18th International Meshing Roundtable*, edited by B. W. Clark, Sandia National Laboratories, Springer Berlin Heidelberg, Berlin, Heidelberg, 2009, pp. 575–594. https://doi.org/10.1007/978-3-642-04319-2_33.

[22] Loseille, A., Dervieux, A., and Alauzet, F., "Fully Anisotropic Goal-Oriented Mesh Adaptation for 3D Steady Euler Equations," *Journal of Computational Physics*, Vol. 229, No. 8, 2010, pp. 2866–2897. https://doi.org/10.1016/j.jcp.2009.12.021.

[23] Belme, A., Alauzet, F., and Dervieux, A., "An a priori Anisotropic Goal-Oriented Error Estimate for Viscous Compressible Flow and Application to Mesh Adaptation," *Journal of Computational Physics*, Vol. 376, 2019, pp. 1051–1088. https://doi.org/10.1016/j.jcp.2018.08.048.

[24] Castro-Diáz, M. J., Hecht, F., Mohammadi, B., and Pironneau, O., "Anisotropic Unstructured Mesh Adaptation for Flow Simulations," *International Journal for Numerical Methods in Fluids*, Vol. 25, No. 4, 1997, pp. 475–491. https://doi.org/10.1002/(SICI)1097-0363(19970830)25:4<475::AID-FLD575>3.0.CO;2-6.

[25] Dompierre, J., Vallet, M.-G., Bourgault, Y., Fortin, M., and Habashi, W. G., "Anisotropic Mesh Adaptation: Towards User-Independent, Mesh-Independent and Solver-Independent CFD. Part III. Unstructured Grids," *International Journal for Numerical Methods in Fluids*, Vol. 39, No. 8, 2002, pp. 675–702. https://doi.org/10.1002/fld.357.

[26] Clément, P., "Approximation by Finite Element Functions using Local Regularization," *ESAIM: Mathematical Modelling and Numerical Analysis - Modélisation Mathématique et Analyse Numérique*, Vol. 9, No. R2, 1975, pp. 77–84. URL http://eudml.org/doc/193271.

[27] George, P.-L., Hecht, F., and Vallet, M.-G., "Creation of Internal Points in Voronoi's Type Method. Control Adaptation," *Advances in Engineering Software and Workstations*, Vol. 13, No. 5–6, 1991, pp. 303–312. https://doi.org/10.1016/0961-3552(91)90034-2.

[28] Alauzet, F., and Frazza, L., "3D RANS Anisotropic Mesh Adaptation on the High-Lift Version of NASA's Common Research Model (HL-CRM)," AIAA Paper 2019–2947, 2019.

[29] Loseille, A., and Löhner, R., "Cavity-Based Operators for Mesh Adaptation," AIAA Paper 2013–152, 2013.

[30] Loseille, A., and Menier, V., "Serial and Parallel Mesh Modification Through a Unique Cavity-Based Primitive," Sandia National Laboratories, Springer International Publishing, 2014, pp. 541–558. https://doi.org/10.1007/978-3-319-02335-9_30.

[31] Loseille, A., Alauzet, F., and Menier, V., "Unique Cavity-Based Operator and Hierarchical Domain Partitioning for Fast Parallel Generation of Anisotropic Meshes," *Computer-Aided Design*, Vol. 85, 2017, pp. 53–67. 24th International Meshing Roundtable Special Issue: Advances in Mesh Generation, https://doi.org/10.1016/j.cad.2016.09.008.

[32] Frey, P. J., "About Surface Remeshing," *9th International Meshing Roundtable*, 2000, pp. 123–136.

[33] Haimes, R., and Drela, M., "On The Construction of Aircraft Conceptual Geometry for High-Fidelity Analysis and Design," AIAA Paper 2012–683, 2012.

[34] Haimes, R., and Dannenhoffer, J. F., III, "EGADSlite: A Lightweight Geometry Kernel for HPC," AIAA Paper 2018–1401, 2018.

[35] Park, M. A., "Anisotropic Output-Based Adaptation with Tetrahedral Cut Cells for Compressible Flows," Ph.D. thesis, Massachusetts Institute of Technology, Sep. 2008. https://doi.org/1721.1/46363.

[36] Freitag, L. A., and Ollivier-Gooch, C., "Tetrahedral Mesh Improvement Using Swapping and Smoothing," *International Journal for Numerical Methods in Engineering*, Vol. 40, 1997, pp. 3979–4002. https://doi.org/10.1002/(SICI)1097-0207(19971115)40:21<3979::AID-NME251>3.0.CO;2-9.

[37] Alauzet, F., "A Changing-Topology Moving Mesh Technique for Large Displacements," *Engineering with Computers*, Vol. 30, No. 2, 2014, pp. 175–200. https://doi.org/10.1007/s00366-013-0340-z.

[38] Bossen, F. J., and Heckbert, P. S., "A Pliant Method for Anisotropic Mesh Generation," Sandia National Laboratories, 1996, pp. 63–74.

[39] Durston, D. A., Cliff, S. E., Denison, M. F., Jensen, J. C., Moran, P. J., Smith, N. T., Heineck, J. T., Schairer, E. T., Kushner, L. K., Castner, R. S., Elmiligui, A. A., Carter, M. B., Winski, C. S., and Shea, P. R., "Nozzle Plume/Shock Interaction Experimental and Computational Sonic Boom Analyses from the NASA Ames 9- by 7-Foot Supersonic Wind Tunnel," NASA TP-2018-219879, Dec. 2018. https://doi.org/2060/20190001341.

[40] Cliff, S. E., Denison, M. F., Moini-Yekta, S., Morr, D. E., and Durston, D. A., "Wind Tunnel Model Design for Sonic Boom Studies of Nozzle Jet Flows with Shock Interactions," AIAA Paper 2016–2035, 2016.

[41] Carter, M. B., and Park, M. A., "Near Field Summary and Analysis of the Third AIAA Sonic Boom Prediction Workshop Shock-Plume Interaction Case," AIAA SciTech 2021 American Institute of Aeronautics and Astronautics, Reston, VA (prepared).

[42] Smith, N. T., Durston, D. A., and Heineck, J. T., "Retroreflective Background Oriented Schlieren Imaging Results from the NASA Plume/Shock Interaction Test," AIAA Paper 2017–43, 2017.

[43] Yates, L. A., "Images Constructed from Computed Flowfields," *AIAA Journal*, Vol. 31, No. 10, 1993, pp. 1877–1884. https://doi.org/10.2514/3.11862.

[44] Heineck, J. T., Banks, D. W., Schairer, E. T., Haering, E. A., Jr., and Bean, P. S., "Background Oriented Schlieren (BOS) of a Supersonic Aircraft in Flight," AIAA Paper 2016–3356, 2016.